






Prediction of Star Formation Rates Using an Artificial Neural Network

Ashraf Ayubinia¹ , Jong-Hak Woo¹ , Fatemeh Hafezianzadeh², Taehwan Kim³, and Changseok Kim¹ 
¹Department of Physics & Astronomy, Seoul National University, Seoul 08826, Republic of Korea; ayubinia_84@snu.ac.kr, jhwoo@snu.ac.kr
²McWilliams Center for Cosmology, Department of Physics, Carnegie Mellon University, Pittsburgh, PA 15213, USA
³Artificial Intelligence Graduate School, UNIST, Ulsan, Republic of Korea

Received 2024 October 30; revised 2024 December 12; accepted 2024 December 20; published 2025 February 12

Abstract

In this study we develop an artificial neural network to estimate the infrared (IR) luminosity and star formation rates (SFR) of galaxies. Our network is trained using “true” IR luminosity values derived from modeling the IR spectral energy distributions of FIR-detected galaxies. We explore five different sets of input features, each incorporating optical, mid-infrared, near-infrared, ultraviolet, and emission line data, along with spectroscopic redshifts and uncertainties. All feature sets yield similar IR luminosity predictions, but including all photometric data leads to slightly improved performance. This suggests that comprehensive photometric information enhances the accuracy of our predictions. Our network is applied to a sample of SDSS galaxies defined as unseen data, and the results are compared with three published catalogs of SFRs. Overall, our network demonstrates excellent performance for star-forming galaxies, while we observe discrepancies in composite and AGN samples. These inconsistencies may stem from uncertainties inherent in the compared catalogs or potential limitations in the performance of our network.

Unified Astronomy Thesaurus concepts: [Galaxies \(573\)](#)

Materials only available in the [online version of record](#): machine-readable table

1. Introduction

The star formation rate (SFR) is a fundamental parameter in galaxy evolution. The star formation process releases energy and new chemical elements that directly impact the evolution of galaxies. Therefore, accurate estimation of SFR is crucial for unraveling the intricate physics underlying galaxy evolution and cosmic star formation history.

A common method of quantifying the SFR of galaxies relies on observations of SFR indicators (J. Moustakas et al. 2006; S. Wuyts et al. 2011; N. M Förster Schreiber & S. Wuyts 2020). In particular, the ultraviolet (UV) continuum emission, which is predominantly emitted by the young stellar populations (which typically fall into the O and B spectral classes), can provide a powerful tool for assessing star formation. Given the short-lived nature of massive stars, the UV continuum is associated with the ongoing star formation activity (~ 100 Myr; S. Salim et al. 2007; V. Buat et al. 2008; L. J. M. Davies et al. 2016). However, employing UV as a diagnostic tool presents several challenges. In addition to the heavy absorption of UV emission by dust (e.g., D. Calzetti et al. 1994), the relationship between UV luminosity and SFR is influenced by gas metallicity (P. Madau & M. Dickinson 2014). Galaxies with higher metallicity emit less UV radiation per unit star formation compared to those with lower metallicity, introducing systematic uncertainty in SFR estimates. Furthermore, the conversion factor from UV luminosity to SFR is not universally fixed, as it can vary depending on various factors, i.e., the stellar initial mass function (IMF; e.g., A. Raiter et al. 2010). These factors contribute to uncertainties in the estimation of SFR (R. C. Kennicutt 1998).

With the advent of large spectroscopic surveys, nebular emission line SFR tracers have been extensively applied to

both local and distant galaxies (e.g., M. Doherty et al. 2006; V. Villar et al. 2008). The $H\alpha$ emission arises from the recombination of interstellar gas ionized by most massive stars ($\gtrsim 15 M_{\odot}$). Hence, $H\alpha$ -based SFR represents the instantaneous measure of the SFR over the past ~ 3 – 10 Myr. The stability of the $H\alpha$ line strength against density or temperature variations makes it one of the most reliable tracers of star formation (R. C. Kennicutt 1998). As the $H\alpha$ emission line moves out of the optical window into the near-infrared (NIR) for objects at high redshifts ($z \gtrsim 0.4$), the [O II] $\lambda 3727$ emission line is frequently adopted as an alternative SFR indicator (e.g., R. C. Kennicutt 1992; D. Rosa-González et al. 2002; B. Argence & F. Lamareille 2009; D. G. Gilbank et al. 2010).

Dust in the ISM introduces additional uncertainty, absorbs UV/optical light, and re-emits it in the form of infrared (IR) radiation. Different physical processes dominate different parts of the IR spectral energy distribution (SED) of galaxies. The diffuse emission from polycyclic aromatic hydrocarbon (PAH) molecules dominates in the $\lambda \sim 3$ – $20 \mu\text{m}$ (M. J. O’Dowd et al. 2009; D. Calzetti 2013). At longer wavelengths, the warm dust continuum, dominated by very small dust grains are stochastically heated by the diffuse interstellar radiation field at high temperatures and prevails in the $\lambda \sim 20$ – $60 \mu\text{m}$ domain (D. Calzetti 2013). Beyond $\sim 60 \mu\text{m}$, the cold dust continuum produced by big dust grains in thermal equilibrium at cool temperatures (about 15–20 K or above; B. T. Draine 2003; J. Falcón-Barroso & J. H. Knapen 2013) dominates. This component is responsible for the bulk of the far-infrared (FIR) emission where the SED peaks. Since the dust absorption cross-section peaks in the UV, the FIR emission becomes a highly sensitive tracer of the young stellar population and SFR. Despite its advantages, the limited sensitivity and spatial resolution of FIR observation facilities have constrained the application of FIR for SFR diagnostics (e.g., T. T. Takeuchi et al. 2010; K. Matsuoka & J.-H. Woo 2015).

Along with massive volumes of astronomical data, machine learning approaches have contributed greatly to the advancement of astronomy (see the reviews by D. Baron 2019; C. J. Fluke & C. Jacobs 2020; M. H. Z. Haghghi 2022; S. A. Webb & S. R. Goode 2023). In addition to the classification (T. Kuntzer et al. 2016; A. O. Clarke et al. 2020; F. Z. Zeraatgari et al. 2024a, and references therein), machine learning is widely applied to regression problems, enabling precise predictions of quantities such as SFR. For example, using a sample of 1136 galaxies in the Herschel-SDSS Strip 82, S. L. Ellison et al. (2016) trained an artificial neural network (ANN) and predicted the total IR luminosity estimates for $\sim 330,000$ SDSS galaxies. Similarly, V. Bonjean et al. (2019) employed Random Forest to estimate SFRs and stellar masses for galaxies at $0.01 < z < 0.3$. Additionally, S. Surana et al. (2020) leveraged deep learning techniques on data from the Galaxy and Mass Assembly (GAMA) survey to estimate stellar masses, SFRs, and dust luminosity. These studies (see also W. Dobbels et al. 2020; A. Narendra et al. 2022; Euclid Collaboration et al. 2023; M. Gai et al. 2024; L. J. Hunt et al. 2024; F. Z. Zeraatgari et al. 2024b) collectively underscore the effectiveness of machine learning in estimating SFRs and related parameters across diverse data sets and methodologies, thus advancing our understanding of galaxy evolution and cosmology.

While SFR estimations based on narrower bands, such as NIR (e.g., C. Neufeld et al. 2024), mid-infrared (MIR, e.g., U. Sureshkumar et al. 2023), and FIR (e.g., V. Picouet et al. 2023), are available, in this study, we employ an artificial neural network on multiband data to estimate total IR luminosity as a key indicator of SFR. By utilizing solely photometric data and incorporating spectroscopic redshift of galaxies, our methodology not only enables the prediction of IR luminosity and SFR for a large population of galaxies but also provides reliable and accurate estimates of SFRs. In Section 2, we explain the data collection process for estimating true IR luminosities and training our network. Section 3 illustrates the structure of our network and the training process. The results are presented in Section 4, and we summarize the application of our neural network on unseen data in Section 5, and we present a summary in Section 6.

2. Data

As we plan to implement our network on the Sloan Digital Sky Survey galaxies, we construct our training sample based on SDSS DR17 (Abdurro’uf et al. 2022). We integrate data from the *photoObj* catalog, which includes photometric data from previous data releases, with spectroscopic data from the *specObj* catalog. This latter catalog incorporates new spectra obtained from the SDSS component of the extended Baryon Oscillation Spectroscopic Survey (eBOSS) for all targets classified as “GALAXY” or “QSO.” The spectroscopic survey observes galaxies with a Petrosian magnitude of $r_{\text{Petro}} < 17.77$ for the main galaxy sample (M. A. Strauss et al. 2002) and $r_{\text{Petro}} < 19.5$ for the luminous red galaxy (LRG) sample (D. J. Eisenstein et al. 2001). We merged the two catalogs by aligning the OBJID in *photoObj* with the “BESTOBJID” in *specObj*. Only targets with reliable redshift measurements are included (ZWARNING = 0). This selection comprises ~ 1.2 million galaxies, which we refer to as our parent sample. After assembling our parent sample, we gather two sets of data. Initially, we acquire FIR and MIR data to model the IR SED of

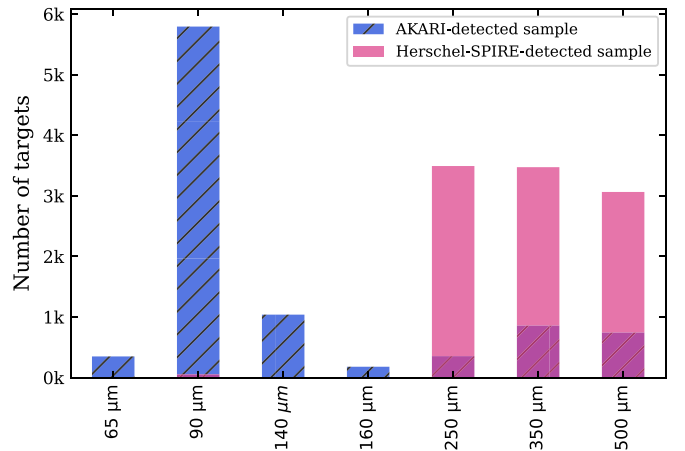


Figure 1. Distribution of FIR-detected galaxies detected by AKARI (blue) and Herschel-SPIRE (red) across various FIR bands.

the training sample, aiming to determine the true values of IR luminosity. Subsequently, we collect additional data to serve as input features for our network, as outlined below.

2.1. IR Data Collection for SED Fitting

The goal of the present study is to predict SFR using IR luminosity. The FIR photometric measurements are crucial to identify IR galaxies whose SEDs peak around $100 \mu\text{m}$. The AKARI FIR all-sky survey carried out by using Far-Infrared Surveyor (FIS; M. Kawada et al. 2007) with superior sensitivity, spatial resolution ($\text{FWHM} = 1' - 1.5'$, Y. Doi et al. 2015) and wider wavelength coverage ($50 - 180 \mu\text{m}$) than the Infrared Astronomical Satellite (IRAS), providing a unique and complementary perspective on the universe. We cross-match our parent sample with the AKARI/FIS bright source catalog version 2 (I. Yamamura et al. 2018), which includes FIR flux measurements for 918,056 IR sources with a matching radius $12''$, corresponding to 2σ positional uncertainty of AKARI. Our target selection requires exceeding the 5σ detection limit in at least one band, which translates to 2.4, 0.55, 1.4, and 6.3 Jy for the 65, 90, 140, and 160 μm bands (M. Kawada et al. 2007), respectively. We obtain 5856 matched targets, of which $\sim 15\%$ are detected in at least one band of the Herschel-SPIRE survey. In addition to AKARI data, we also utilize the Herschel FIR data to increase the size of FIR-detected galaxies. To do this, we cross-match our parent sample with the Herschel Stripe 82 Survey (HerS, M. P. Viero et al. 2014). HerS covers approximately half of the 150 deg^2 of the deep SDSS Stripe, providing a $250 \mu\text{m}$ -selected catalog of 3.3×10^4 sources detected at $>3\sigma$ (including confusion noise), where the completeness is estimated to be 50% and the false detection rate to be less than 1% (M. P. Viero et al. 2014). We find that 3540 galaxies from our parent sample are included in this catalog, of which $\sim 3\%$ are detected in at least one band of the AKARI survey. We eliminate 48 targets already included in the AKARI-detected sample. Figure 1 illustrates the distribution of 9348 FIR-detected galaxies across various FIR bands.

The MIR data of our FIR-detected galaxies are collected from Wide-field Infrared Survey Explorer (WISE; E. L. Wright et al. 2010), which surveyed the entire sky in four infrared wavelengths of 3.4, 4.6, 12, and 22 μm (hereafter W1, W2, W3, and W4). We eliminate sources flagged as either spurious (created by diffraction spikes or astrophysical sources with

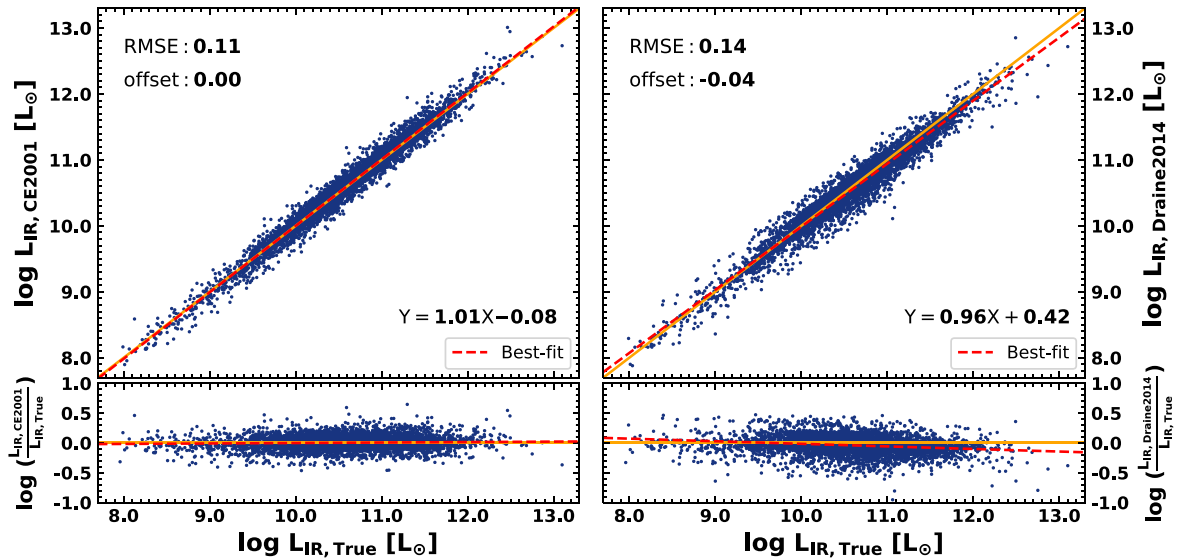


Figure 2. Comparison between true IR luminosity estimated using the model presented in C. M. Casey (2012) with those estimated from templates described in R. Chary & D. Elbaz (2001; left panel) and B. T. Draine et al. (2014; right panel). The red dashed line shows one-to-one correlation. The orange line represents the one-to-one correlation, and the red dashed line indicates the best fit. The equation of the best fit is displayed on each plot.

photometry contaminated by diffraction spikes) or as contaminated by moonlight in the AllWISE catalog. Additionally, some objects with null values for flux uncertainties are removed from the sample. It results in 7162 IR galaxies suitable for fitting their IR SEDs.

2.1.1. Estimation of True IR Luminosity

To obtain true values of IR luminosity for our training sample, we fit the IR component of the SEDs using IR flux measurements from the AKARI and Herschel surveys. When IRAS data are available, we include them to further improve the accuracy and quality of our fits. In this process, various IR templates are employed through CIGALE fitting to accurately model the SEDs.

In CIGALE, there are different IR templates (B. T. Draine & A. Li 2007; D. A. Dale et al. 2014; B. T. Draine et al. 2014). In this study, we estimate dust luminosity using the model described in C. M. Casey (2012). This model integrates a modified blackbody with a MIR continuum power law, effectively addressing both large-scale cold dust emission and warm dust emission. We note that while this fitting technique does not account for PAH emission in the MIR, as its influence on integrated FIR properties is negligible (C. M. Casey 2012), it has been shown to perform well in both the case of sources with or without active galactic nuclei (AGN; T. T. Shimizu et al. 2015).

To ensure consistency in our SED fitting results, we use two additional dust templates. First, we fit the IR SEDs using the Chary-Elbaz IR template library (R. Chary & D. Elbaz 2001), which includes 105 templates based on data from the IR Space Observatory (ISO; M. F. Kessler et al. 1996), IRAS, and SCUBA. These templates cover a wide range of IR luminosities from normal star-forming galaxies to ultraluminous infrared galaxies (ULIRGs) but do not account for AGN contributions, so we exclude W1, W2, and W3 data. Second, we use the models from B. T. Draine & A. Li (2007) and B. T. Draine et al. (2014), which feature a dust mixture of amorphous silicate, graphite grains, and PAHs. These models

distinguish between diffuse and star-forming dust components, with the 2014 update offering a variable power-law index and expanded radiation field ranges for more accurate and flexible fitting of IR data.

Figure 2 compares IR luminosity estimates derived from three different sets of templates. The small scatter, indicated by the low root mean square error (RMSE), which quantifies the average magnitude of deviations between predicted values and actual outcomes, along with the negligible offset between estimates, indicates minimal deviations. This demonstrates the consistency in IR luminosity estimates and suggests they are not strongly dependent on the choice of IR templates. Hence, we can proceed confidently with the results obtained from the template provided by C. M. Casey (2012) using CIGALE (M. Boquien et al. 2019; G. Yang et al. 2020).

2.2. Data Collection for Training Network

In the realm of neural networks, the term “features” refers to the input variables that neural networks process during the training phase to determine patterns, relationships, and representations within the data. In our study, we present five sets of features, evaluating the performance of the network in each case. Motivated by previous studies attempting to estimate SFR using machine learning techniques (S. L. Ellison et al. 2016; V. Bonjean et al. 2019; S. Surana et al. 2020), our initial training involves the primary feature set, encompassing optical and MIR photometric data, along with SDSS redshift, and their corresponding errors. Despite training our network with photometric redshift as well, the results showed minimal change, reinforcing our decision to prioritize spectroscopic redshift due to its higher accuracy.

Subsequently, we incorporate additional features including NIR and UV photometry as well as emission lines in a stepwise manner, each time retraining the network with the augmented data (see Table 1). We collect NIR and UV photometric data from the Two Micron All Sky Survey (2MASS, J. Huchra et al. 2005; J. P. Huchra et al. 2012) and Galaxy Evolution Explorer (GALEX, D. C. Martin et al. 2005; L. Bianchi 2014) using a

Table 1
List of Feature Sets

Primary Features	NIR Features	UV Features	Emission Line Features
z : redshift	$J-H$	FUV-NUV	Luminosity of [O II] $\lambda 3727 \text{ \AA}$ emission line
M_u : absolute u -band magnitude	$H-K$		Luminosity of [O II] $\lambda 3729 \text{ \AA}$ emission line
M_g : absolute g -band magnitude	$J-K$		Luminosity of [O III] $\lambda 4959 \text{ \AA}$ emission line
M_r : absolute r -band magnitude			Luminosity of [O III] $\lambda 5007 \text{ \AA}$ emission line
M_i : absolute i -band magnitude			Luminosity of H α $\lambda 6563 \text{ \AA}$ emission line
M_z : absolute z -band magnitude			Luminosity of H β $\lambda 4861 \text{ \AA}$ emission line
$u-g$			Luminosity of [N II] $\lambda 6582 \text{ \AA}$ emission line
$g-r$			Luminosity of [N II] $\lambda 6582 \text{ \AA}$ emission line
$r-i$			Luminosity of [S II] $\lambda 6717 \text{ \AA}$ emission line
$i-z$			Luminosity of [S II] $\lambda 6731 \text{ \AA}$ emission line
w1-w2			
w2-w3			
w3-w4			

Note. Column (1): The primary features. Columns (2)–(4): NIR colors, UV colors, and emission lines, respectively. We incorporated additional features including NIR and UV photometric colors as well as emission lines in a stepwise manner, each time retraining the network with the augmented data.

searching radius of $12''$. Emission line fluxes are taken from the MPA-JHU catalog (K. N. Abazajian et al. 2009). To ensure robustness, we exclude targets with measurements carrying significant uncertainties exceeding 3σ , thereby refining the data set for more reliable model training. As a result, we have a sample of 6426 FIR-detected sources with the primary feature set as input data. This sample is divided into training and validation sets, with 80% allocated for training and 20% for validation (see Section 3). Figure 3 shows the distribution of features for both the training and validation data sets.

3. Artificial Neural Network Model

Our objective is to design a network capable of predicting IR luminosity accurately. After exploring various machine learning models such as XGBoost and Random forest, we find that a simple ANN exhibits the most promising performance on our data. ANNs (R. E. Uhrig 1995; A. Abraham 2005) are computational models inspired by the structure and function of the human brain. They are highly effective at identifying patterns and revealing intricate relationships in data, primarily serving three key functions; regression (as shown in this study), classification, and control/optimization. These networks are built using layers of interconnected processing units called artificial neurons. Each neuron receives information, performs calculations, and transmits the results to the next layer. A key strength of neural networks is their ability to model complex, nonlinear relationships without needing preexisting knowledge about the structure of data. However, building an effective neural network requires experimentation. This involves fine-tuning various parameters such as the number of neurons, activation functions, learning rate, training iterations (epochs), optimization algorithms, and regularization techniques to prevent overfitting.

Our model is designed as a multilayer perceptron (MLP) that comprises one input layer, one hidden layer, and one output layer. The layer contains 128 neurons and takes the input directly, processing it to produce the output. This simple structure leverages the ability of the dense layer to model complex relationships in the data, even with a straightforward configuration. Each neuron uses the rectified linear unit (ReLU; Y. LeCun et al. 2015; A. F. Agarap 2018) activation function, which performs a nonlinear transformation on the

output received from the previous layer. Our regression model employs a linear activation function in the output layer, enabling continuous value prediction. Note that while this allows for potentially unbounded output, other model factors may influence the actual range. Additionally, the He uniform initializer (K. He et al. 2016) is used to initialize the weights of the layers, and L1 and L2 regularization is applied to each layer to prevent overfitting by penalizing large weights.

The model is optimized using the mean squared error (MSE) loss function and the Adam optimizer, a stochastic gradient descent (SGD) variant. Adam adapts the learning rate by estimating first-order moments (the mean of the gradients) and second-order moments (the uncentered variance of the gradients). This allows Adam to perform well in various situations, especially when dealing with sparse gradients or noisy data, by adjusting the learning rate dynamically for each parameter during training (D. P. Kingma & J. Ba 2015). The initial learning rate is set to 0.001. The model evaluates its performance using multiple metrics, including MSE, RMSE, and R^2 score (that indicates the proportion of the variance in the dependent variable that is predictable from the independent variables), all of which are considered important for assessing the performance of the model. To effectively monitor the performance of our model during training and to combat local minima in the loss function, we employ two key techniques. First, we dynamically adjust the learning rate by reducing it when the validation loss plateaus. Second, we implement early stopping, which halts training if the validation loss fails to improve over a specified number of epochs. We split our input data (6246 FIR-detected sources) into training and validation sets, allocating 80% for training and 20% for validation in each run. Using the training data, the model is trained, and then its performance is evaluated using the validation data. Model refinement and enhancement are driven by the error calculated on the validation set, guiding iterative improvements.

4. Results

This section presents the results of all experiments conducted using the aforementioned architecture. Table 2 shows the results for each model, including different sets of input features. To ensure the robustness of our training process and avoid local minima, we trained each network 10 times. The

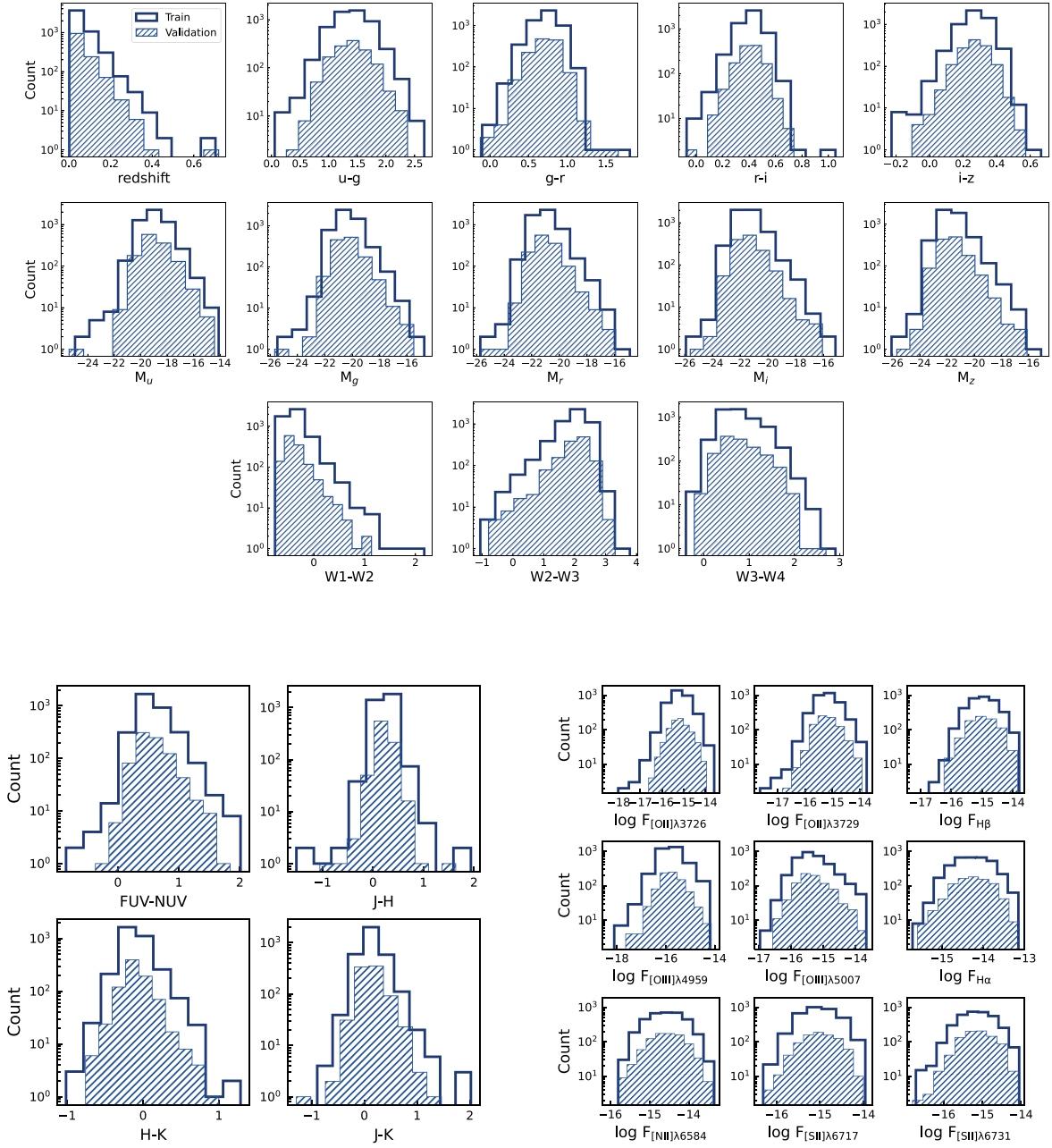


Figure 3. The distribution of the primary (top), NIR and UV (bottom left), and emission line (bottom right) features for training data (solid histograms) and the validation data (dashed histograms). Magnitudes are in the AB system and the emission line flux unit is $\text{erg cm}^{-2} \text{s}^{-1}$.

differences between these iterations are negligible, suggesting that our models are robust. Therefore, we consider the best results from each network.

Although all five feature sets exhibit identical overall performance, the output from the network shows slightly better statistical metrics of both training and unseen data when all photometric features are utilized (particularly in the case of star-forming galaxies, see Table 2). Hence, this particular model (i.e., main model in Table 2) is preferable due to its better performance, which includes a higher R^2 score and lower MSE on both training and test sets.

The loss function serves as a crucial metric that quantifies the disparity between the true values and the predictions generated by the network during the training process. During training, the network iteratively adjusts its parameters to minimize the loss

function, effectively fine-tuning its predictive capabilities. A decreasing trend in the loss function over epochs indicates that the network is learning to better approximate the true values. Figure 4 illustrates the loss function for our main model. In our training process, we employ a learning rate reduction strategy where the learning rate decreases by a factor of 0.1. This reduction factor is applied periodically during training epochs. By gradually decreasing the learning rate, we allow the optimization process to converge more effectively toward an optimal solution, potentially preventing overshooting of the minimum loss. This strategy often helps improve the stability and convergence of the training process, leading to better generalization performance on unseen data.

In Figure 5, outputs of four models are scrutinized against those of the main reference model, encompassing both training

Table 2
The Statistical Results of Our Trained Network Using Different Feature Sets

Model	Network					Unseen Data			
	# Sample	R^2_{Train}	R^2_{Val}	$\text{MSE}_{\text{Train}}$	MSE_{Val}	Class	MPA-JHU	Salim18	Ellison16
Model 1	6426	96%	95%	0.0160	0.0210	SFGs	(0.28, -0.04)	(0.21, 0.03)	(0.14, 0.03)
Optical + MIR						Composites	(0.57, -0.4)	(0.30, -0.18)	(0.18, 0.03)
26 features						AGNs	(0.83, -0.68)	(0.44, -0.31)	(0.23, 0.02)
Model 2	5865	97%	95%	0.0141	0.0201	SFGs	(0.29, -0.09)	(0.20, -0.01)	(0.14, 0.00)
Optical + MIR + NIR						Composites	(0.58, -0.42)	(0.31, -0.19)	(0.17, 0.02)
32 features						AGNs	(0.85, -0.70)	(0.45, -0.32)	(0.21, 0.00)
Model 3	4703	97%	95%	0.0132	0.0215	SFGs	(0.24, -0.06)	(0.18, 0.02)	(0.15, 0.02)
Optical + MIR + UV						Composites	(0.47, -0.32)	(0.25, -0.14)	(0.17, 0.02)
28 features						AGNs	(0.73, -0.57)	(0.34, 0.22)	(0.21, 0.01)
Model 4	4233	94%	90%	0.0135	0.0215	SFGs	(0.27, -0.02)	(0.21, 0.06)	(0.14, 0.06)
Optical + MIR + Emission lines						Composites	(0.54, -0.37)	(0.29, -0.15)	(0.17, 0.06)
44 features						AGNs	(0.82, -0.66)	(0.42, -0.28)	(0.20, 0.04)
Main Model	4190	97%	96%	0.0119	0.0186	SFGs	(0.19, -0.02)	(0.17, 0.02)	(0.15, -0.02)
Optical + MIR + NIR + UV						Composites	(0.48, -0.33)	(0.25, -0.14)	(0.17, 0.02)
34 features						AGNs	(0.71, -0.55)	(0.35, -0.24)	(0.23, 0.01)

Note. Column (1): Name of model and the number of features. Column (2): Size of sample (training plus validation data). Columns (3)–(4): R^2 score for training data and validation data. Columns (5)–(6): Mean square error (MSE) for training data and validation data. Column (7): target classification based on MPA-JHU catalog. Columns (8)–(10): In each cell, the top number represents the RMSE, while the bottom number indicates the offset between the values provided by the catalogs and the predicted SFRs (see Figure 7).

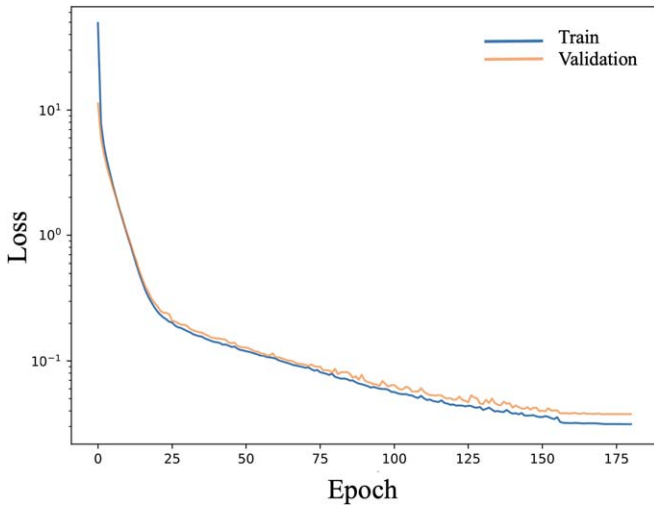


Figure 4. The loss function for training (blue) and validation (orange) data as a function of epoch for the main model network. The gap between the loss function of the training and validation is negligible.

and validation data sets. It is clear that these models provide consistent results with marginal offsets and scatters. Following these comparisons, we proceed with our analysis using the main model.

In Figure 6, we compare the true IR luminosities estimated from SED fitting with those predicted using the main feature set. The close alignment of the one-to-one correlation (yellow line) with the best fit (red dashed line), with slopes of 0.96 for the training data and 0.94 for the validation data, indicates a strong linear relationship between the variables. This alignment is supported by small RMSE values and no offset, indicating precise predictions across the data set. However, minor

deviations are observed where predictions slightly exceed true values at lower IR luminosities and slightly underestimate them at higher luminosities. Despite these minor deviations, our network estimates IR luminosity with uncertainties of 0.22 dex for the training data and 0.26 dex for the validation data, both at a 95% confidence level, considering the normal distribution of residuals (predicted values—true values) for both training and validation data. This demonstrates that the model has successfully learned the complex relationships between input features and IR luminosity, leading to good predictions across both training and validation sets.

5. Discussion

In this section, we explore how well our network generalizes to unseen data that the model has not encountered during the training process, ensuring it extends beyond the training set. We convert the predicted IR luminosities obtained from our main model (see Table 2) into star formation rates (SFR_{ANN}) using the modified equation for a Chabrier IMF:

$$\log \text{SFR}(M_{\odot} \text{yr}^{-1}) = \log L_{\text{IR}}(\text{erg s}^{-1}) - 43.591. \quad (1)$$

We validate our model by comparing its predictions of SFRs with those from three specific catalogs: the MPA-JHU value-added catalog based on DR8, the GALEX-SDSS-WISE Legacy Catalog (GSWLC-2, S. Salim et al. 2016, 2018), and the catalog provided by S. L. Ellison et al. (2016). These catalogs were chosen for their comprehensive size and because they are primarily based on SDSS data. Importantly, all input features used in our main network are available for the majority of targets in these catalogs, enabling us to apply our model to them. Additionally, each catalog provides independent SFR estimations, ensuring that the performance of our model can be evaluated against other SFR indicators. By evaluating our model on these data sets, we assess its reliability in predicting SFRs for new, unseen data, highlighting its potential for

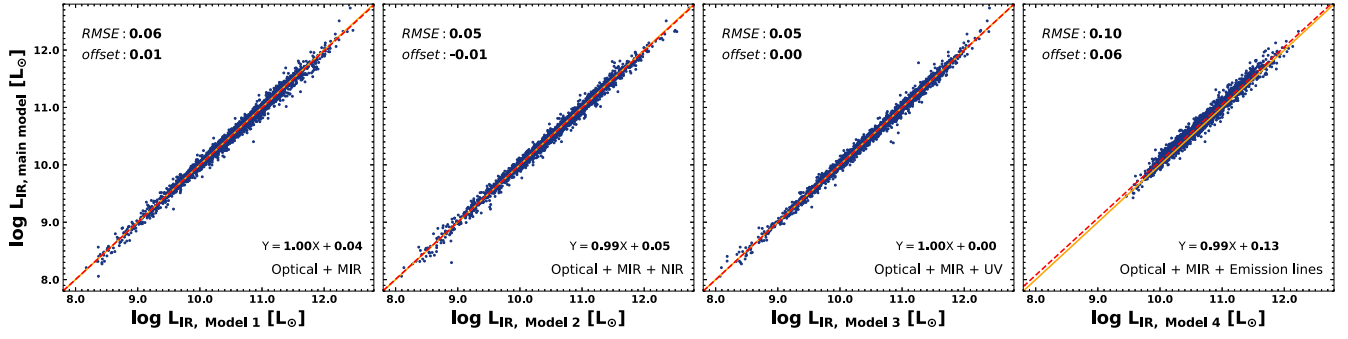


Figure 5. Comparison between IR luminosity estimated using the mainT model (Y -axis) with those estimated from other models (x -axis). Model 1: Optical + MIR; Model 2: Optical + MIR + NIR; Model 3: Optical + MIR + UV, Model 4: Optical + MIR + emission lines. The orange line represents the one-to-one correlation, and the red dashed line indicates the best fit. The equation of the best fit is displayed on each plot.

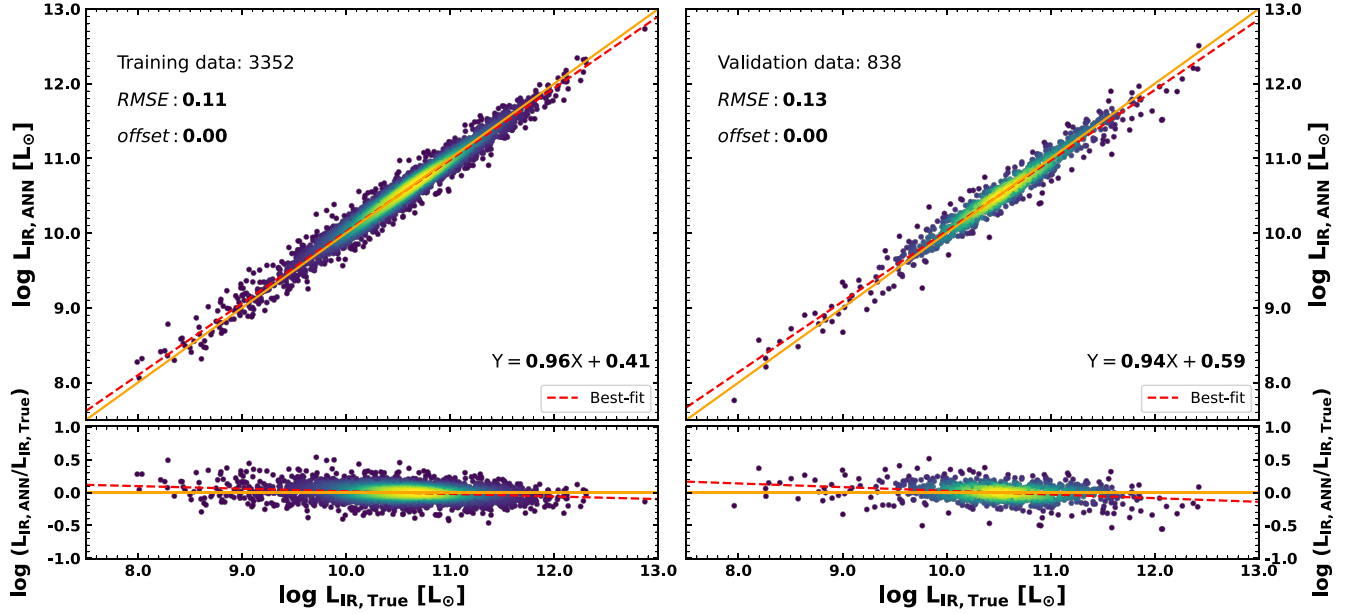


Figure 6. The comparison between the true IR luminosities estimated from SED fitting with those predicted using the main model for training data (left) and validation data (right) sets. The orange line presents the one-to-one correlation and the red dashed line indicates the best fit. The equation of the best fit is displayed on each plot.

broader astrophysical research. In the following, we describe these catalogs in detail, explain the construction of our unseen sample, and discuss our results.

First, the MPA-JHU catalog offers SFR measurements based on $H\alpha$ emission line flux corrected for dust extinction that can obscure star formation activity using the Balmer decrement for galaxies classified as star-forming according to the BPT diagram (J. A. Baldwin et al. 1981). For AGNs or galaxies lacking significant emission lines, SFRs are alternatively derived from the relation between the 4000 \AA break strength ($D_n4000 \text{ \AA}$) and SFR, following methods such as those outlined by G. Kauffmann et al. (2003). Additionally, all SFR measures in the MPA-JHU catalog are adjusted for fiber aperture effects, which is crucial for providing consistent SFR estimates across different parts of the galaxies. These SFR estimates initially assume a Kroupa IMF but are then recalibrated to a Chabrier IMF, ensuring compatibility with other commonly used stellar population models. We focus on targets classified as star-forming, composite, and AGN in this catalog.

Second, we utilize the GSWLC-2 catalog, the second version of GSWLC that provides SFR values obtained from UV/

optical SED fitting and mid-IR SFRs derived from IR templates based upon $22 \mu\text{m}$ WISE observations. As these mid-IR SFRs tend to be overestimated for galaxies with AGN, likely due to nonstellar dust heating (S. Salim et al. 2016), we adopt the UV/optical SFRs for our comparisons. We exclude targets with flagged SEDs in the GSWLC-2 catalog.

Third, we utilize a catalog containing predicted total IR luminosities for a substantial number of SDSS galaxies. These IR luminosities are estimated using an ANN that incorporates 23 input optical parameters, including continuum and emission line fluxes (S. L. Ellison et al. 2016). These estimates are the most relevant for comparison with our network. We convert the total IR luminosity into SFR using Equation (1). We prioritize targets with more reliable SFR estimates (i.e., $\sigma_{\text{ANN}} < 0.1$) as suggested by S. L. Ellison et al. (2016).

We note that for each catalog, we collect and clean the data using the same process applied to the input data. To ensure a fair comparison of our learning model across these catalogs, we cross-correlate the samples before applying the model, resulting in the selection of the same individual objects and an equal number of targets across the data sets. This involves

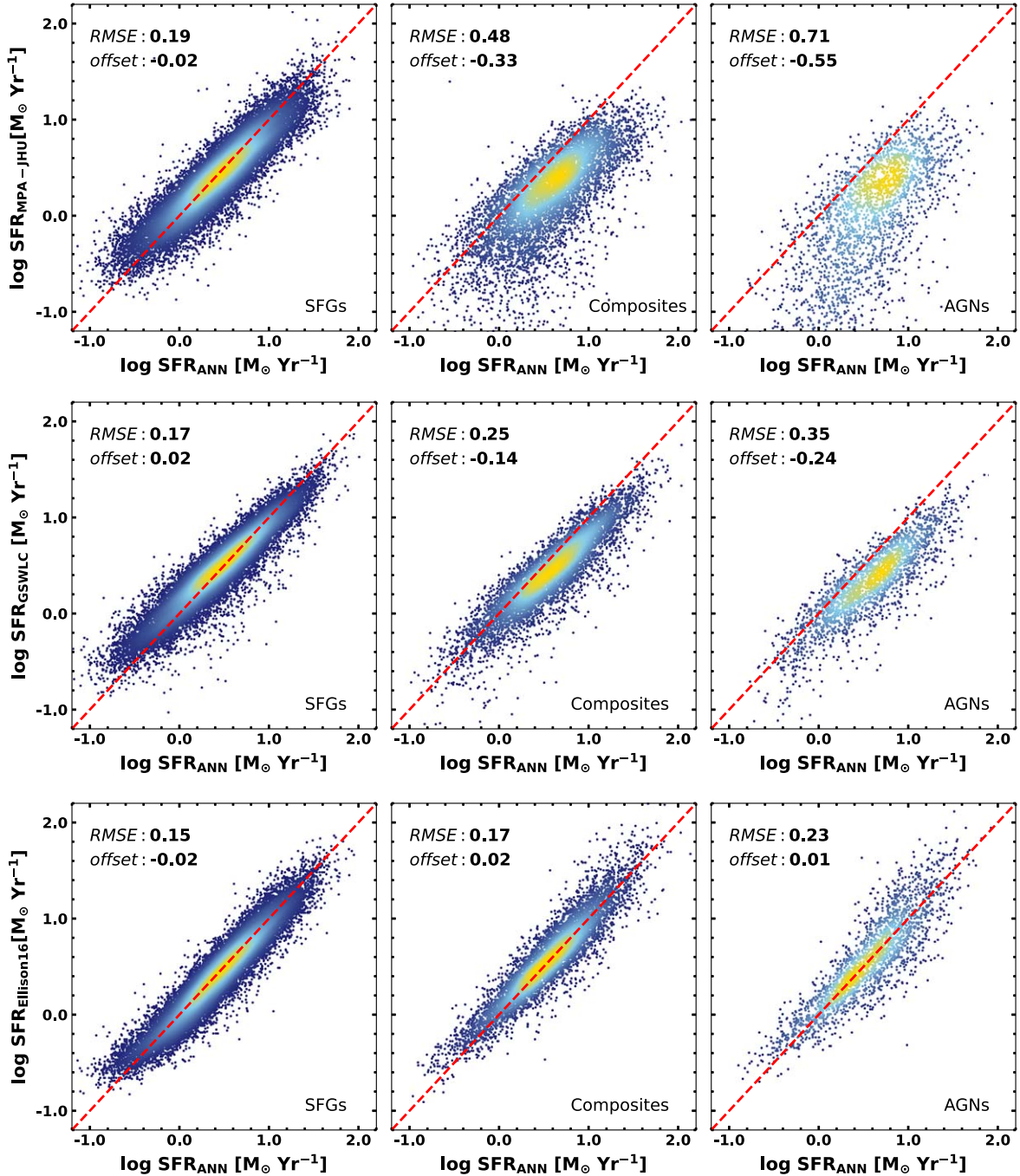


Figure 7. The comparison between our ANN results (X-axis) with MPA-JHU catalog (top row), GSWLC-2 catalog (middle row) and ANN trained by S. L. Ellison et al. (2016; bottom row) for star-forming galaxies, composites, and AGNs.

aligning and standardizing the data to eliminate inconsistencies and ensuring that each sample is directly comparable under the same conditions. This yields ~ 45 k targets.

Likewise, in Figure 7, we compare our network output with SFRs from these catalogs. For this comparison, we divide the sample into star-forming galaxies, composite galaxies, and AGNs to explore any systematic differences arising from AGN activity, which can influence SFR measurements due to contamination from nonstellar emission. The top row compares our network predictions and the MPA-JHU catalog. For star-forming galaxies (left panel), there is an excellent agreement between the predicted

and observed SFRs, with an $\text{RMSE} \sim 0.2$ dex and $\text{offset} = 0.02$ dex. This result underscores the good performance of our network in accurately predicting SFRs for galaxies dominated by star-forming processes. In our training data, star-forming galaxies are the most represented, followed by composite galaxies, with AGNs having the fewest targets. This imbalance likely contributes to the better performance of ANN for star-forming galaxies. Additionally, the well-modeled IR SEDs of star-forming galaxies provide more reliable true SFR values for training the model. Together, these factors enhance the ability of our network to generalize and predict accurately for this galaxy population.

However, the agreement is less robust for composite galaxies (middle panel), with an RMSE ~ 0.5 dex and an offset of 0.33 dex. These discrepancies might stem from the dual contributions of star formation and AGN activity in composite galaxies, which complicate the determination of accurate SFRs.

For AGNs (right panel), the RMSE increases to ~ 0.7 dex, with a significant offset of 0.55 dex. The larger scatter and systematic offset may arise from the considerable uncertainties associated with using D_n4000 -based SFR estimates for AGN-hosting galaxies, as AGN activity can dominate or obscure the spectral features tied to star formation. Alternatively, these discrepancies could point to limitations in the ability of our ANN to predict IR luminosities accurately in galaxies with prominent AGN activity, potentially due to insufficient training data or inherent complexities in the underlying physics of AGN-dominated systems.

In the middle row, we present the comparisons between our neural network and the GSWLC-2 catalog. For star-forming galaxies (left panel), there is good agreement, with RMSE ~ 0.2 and offset = 0.02 dex, indicating consistent performance. However, for composite galaxies (middle panel), there are still some discrepancies, reflected by an RMSE ~ 0.25 and offset = 0.14 dex. Despite some improvements, noticeable offsets persist for AGNs (right panel), with an RMSE ~ 0.3 and an offset of 0.24 dex, suggesting that further refinement may be required.

The bottom row depicts the comparison between the output of our network and the SFR predicted by the ANN trained by S. L. Ellison et al. (2016). We observe excellent agreement between the two networks for all galaxies. However, the superiority of our network lies in its ability to be applied to a larger population of galaxies. This is because we trained our network without relying on emission line measurements, which require reliable spectra.

Overall, our neural network demonstrates good performance, particularly for star-forming galaxies, where it consistently predicts SFRs with minimal discrepancies compared to established catalogs. While some offsets persist for composite galaxies and AGNs, these discrepancies might be attributed to the lack of accurate estimations in the catalogs or insufficient training of our network due to the small number of composite galaxies and AGNs in the training data or because the IR SEDs for these types may not be well-modeled. This issue could be addressed in future developments by including larger, more balanced data sets with better class representation, which would enhance the ability of the trained model to predict SFRs across all galaxy types. The current study suggests that further refinement may be required but also emphasizes the robustness of our model, particularly in its ability to generalize across different galaxy populations.

6. Summary

In this study, we develop and train an artificial neural network using a data set of FIR-detected galaxies to accurately predict their IR luminosities. We explore five distinct sets of input features, including optical and MIR photometric data,

SDSS redshift, and their corresponding errors. Subsequently, we incorporate additional features, such as NIR and UV photometry, as well as emission lines, in a stepwise manner. Each time, we retrain the network with the augmented data (see Table 1).

Our findings reveal that all sets of features yield comparable predictions of IR luminosity. Interestingly, incorporating all available photometric data led to an improvement in the predictive performance of our network, particularly in the case of star-forming galaxies. This suggests that integrating diverse photometric measurements enhances the ability of the model to capture the complex relationships between different spectral regions and the IR luminosities of galaxies.

While the performance of our network closely resembles that of the previous study by S. L. Ellison et al. (2016), our distinct approach employing solely photometric data enables its application to a broader range of galaxies, enhancing its utility across a large population of galactic systems.

Acknowledgments

This work has been supported by the Basic Science Research Program through the National Research Foundation of the Korean Government (grant No. 2021R1A2C3008486) and Institute of Information & communications Technology Planning & Evaluation (IITP) grant funded by the Korea government (MSIT) (No.RS-2021-II212068, Artificial Intelligence Innovation Hub). This research has made use of the NASA/IPAC Extragalactic Database (NED), which is operated by the Jet Propulsion Laboratory, California Institute of Technology, under contract with the National Aeronautics and Space Administration.

Software: CIGALE (M. Boquien et al. 2019; G. Yang et al. 2020), Astropy (Astropy Collaboration et al. 2013, 2018, 2022), Tensorflow (M. Abadi et al. 2016), Scikit-learn (F. Pedregosa et al. 2011).

Data availability: The predicted values of IR luminosity by our ANN for unseen data are publicly available in the online journal (Appendix, Table 3).

Appendix Unseen Data

Table 3 summarizes the unseen data available in the online journal.

Units	Label	Description
...	Index	Sequential index of object in table
deg	RAdeg	R.A., decimal degrees (J2000)
deg	DEdeg	Decl., decimal degrees (J2000)
...	z	SDSS spectroscopic redshift
$[L_{\odot}]$	logLIRpred	log, predicted IR luminosity in solar units

(This table is available in its entirety in machine-readable form in the [online article](#).)

ORCID iDs

Ashraf Ayubinia  <https://orcid.org/0009-0002-9526-5820>
 Jong-Hak Woo  <https://orcid.org/0000-0002-8055-5465>
 Changseok Kim  <https://orcid.org/0000-0002-2156-4994>

References

- Abazajian, K. N., Adelman-McCarthy, J. K., Agüeros, M. A., et al. 2009, *ApJS*, **182**, 543
- Abadi, M., Barham, P., Chen, J., et al. 2016, in Proc. 12th USENIX Symp. on Operating Systems Design and Implementation (OSDI), 16, 265
- Abdurro'uf, Accetta, K., Aerts, C., et al. 2022, *ApJS*, **259**, 35
- Abraham, A. 2005, in Artificial Neural Networks. Handbook of Measuring System Design, ed. P. H. Sydenham & R. Thorn (Hoboken, NJ: John Wiley & Sons)
- Agarap, A. F. 2018, arXiv:1803.08375
- Argence, B., & Lamareille, F. 2009, *A&A*, **495**, 759
- Astropy Collaboration, Price-Whelan, A. M., Lim, P. L., et al. 2022, *ApJ*, **935**, 167
- Astropy Collaboration, Price-Whelan, A. M., Sipőcz, B. M., et al. 2018, *AJ*, **156**, 123
- Astropy Collaboration, Robitaille, T. P., Tollerud, E. J., et al. 2013, *A&A*, **558**, A33
- Baldwin, J. A., Phillips, M. M., & Terlevich, R. 1981, *PASP*, **93**, 5
- Baron, D. 2019, arXiv:1904.07248
- Bianchi, L. 2014, *Ap&SS*, **354**, 103
- Boquien, M., Burgarella, D., Roehlly, Y., et al. 2019, *A&A*, **622**, A103
- Bonjean, V., Aghanim, N., Salomé, P., et al. 2019, *A&A*, **622**, A137
- Buat, V., Boissier, S., Burgarella, D., et al. 2008, *A&A*, **483**, 107
- Calzetti, D. 2013, *Secular Evolution of Galaxies* (Cambridge: Cambridge Univ. Press), 419
- Calzetti, D., Kinney, A. L., & Storchi-Bergmann, T. 1994, *ApJ*, **429**, 582
- Casey, C. M. 2012, *MNRAS*, **425**, 3094
- Chary, R., & Elbaz, D. 2001, *ApJ*, **556**, 562
- Clarke, A. O., Scaife, A. M. M., Greenhalgh, R., et al. 2020, *A&A*, **639**, A84
- Dale, D. A., Helou, G., Magdis, G. E., et al. 2014, *ApJ*, **784**, 83
- Davies, L. J. M., Driver, S. P., Robotham, A. S. G., et al. 2016, *MNRAS*, **461**, 458
- Doi, Y., Takita, S., Ootsubo, T., et al. 2015, *PASJ*, **67**, 50
- Dobbels, W., Baes, M., Viaene, S., et al. 2020, *A&A*, **634**, A57
- Draine, B. T. 2003, *ARA&A*, **41**, 241
- Draine, B. T., Aniano, G., Krause, O., et al. 2014, *ApJ*, **780**, 172
- Draine, B. T., & Li, A. 2007, *ApJ*, **657**, 810
- Doherty, M., Bunker, A., Sharp, R., et al. 2006, *MNRAS*, **370**, 331
- Eisenstein, D. J., Annis, J., Gunn, J. E., et al. 2001, *AJ*, **122**, 2267
- Ellison, S. L., Teimoorinia, H., Rosario, D. J., & Mendel, J. T. 2016, *MNRAS*, **455**, 370
- Euclid Collaboration, Bisigello, L., Conselice, C. J., et al. 2023, *MNRAS*, **520**, 3529
- Falcn-Barroso, J., & Knapen, J. H. 2013, *Secular Evolution of Galaxies* (Cambridge: Cambridge Univ. Press),
- Fluke, C. J., & Jacobs, C. 2020, *WDMKD*, **10**, e1349
- Förster Schreiber, N. M., & Wuyts, S. 2020, *ARA&A*, **58**, 661, Mario Gai, Mario Bove, Giovanni Bonetta, Davide Zago, Rossella Cancelliere
- Gai, M., Bove, M., Bonetta, G., Zago, D., & Cancelliere, R. 2024, *MNRAS*, **532**, 1391
- Gilbank, D. G., Baldry, I. K., Balogh, M. L., et al. 2010, *MNRAS*, **405**, 2594
- Haghighi, M. H. Z. 2022, *A&AT*, **33**, 323
- He, K., Zhang, X., Ren, S., & Sun, J. 2016, in IEEE Conf. on Computer Vision and Pattern Recognition (Piscataway, NJ: IEEE), 770
- Huchra, J., Martimbeau, N., Jarrett, T., et al. 2005, in IAU Symp. 216, Maps of the Cosmos, ed. M. Colless, L. Staveley-Smith, & R. A. Stathakis (Cambridge: Cambridge Univ. Press), 170
- Huchra, J. P., Macri, L. M., Masters, K. L., et al. 2012, *ApJS*, **199**, 26
- Hunt, L. J., Pimblet, K. A., & Benoit, D. M. 2024, *MNRAS*, **529**, 479
- Kauffmann, G., Heckman, T. M., White, S. D. M., et al. 2003, *MNRAS*, **341**, 33
- Kawada, M., Baba, H., Barthel, P. D., et al. 2007, *PASJ*, **59**, S389
- Kennicutt, R. C. 1998, *ARA&A*, **36**, 189
- Kennicutt, R. C. 1992, *ApJ*, **388**, 310
- Kessler, M. F., Steinz, J. A., Anderegg, M. E., et al. 1996, *A&A*, **315**, L27
- Kingma, D. P., & Ba, J. 2015, arXiv:1412.6980
- Kuntzer, T., Tewes, M., Courbin, F., et al. 2016, *A&A*, **591**, A54
- O'Dowd, M. J., Schiminovich, D., Johnson, B. D., et al. 2009, *ApJ*, **705**, 885
- LeCun, Y., Bengio, Y., & Hinton, G. 2015, *Natur*, **521**, 436
- Madau, P., & Dickinson, M. 2014, *ARA&A*, **52**, 415
- Martin, D. C., Fanson, J., Schiminovich, D., et al. 2005, *ApJL*, **619**, L1
- Moustakas, J., Kennicutt, R. C., & Tremonti, C. A. 2006, *ApJ*, **642**, 775
- Matsuoka, K., & Woo, J.-H. 2015, *ApJ*, **807**, 28
- Narendra, A., Gibson, S. J., Dainotti, M. G., et al. 2022, *ApJS*, **259**, 55
- Neufeld, C., van Dokkum, P., Asali, Y., et al. 2024, *ApJ*, **972**, 156
- Pedregosa, F., Varoquaux, G., Gramfort, A., et al. 2011, *JMLR*, **12**, 2825
- Picouet, V., Arnouts, S., Le Floch, E., et al. 2023, *A&A*, **675**, A164
- Raiter, A., Schaerer, D., & Fosbury, R. A. E. 2010, *A&A*, **523**, A64
- Rosa-González, D., Terlevich, E., & Terlevich, R. 2002, *MNRAS*, **332**, 283
- Salim, S., Boquien, M., & Lee, J. C. 2018, *ApJ*, **859**, 11
- Salim, S., Lee, J. C., Janowiecki, S., et al. 2016, *ApJS*, **227**, 2
- Salim, S., Rich, R. M., Charlot, S., et al. 2007, *ApJS*, **173**, 267
- Shimizu, T. T., Mushotzky, R. F., Meléndez, M., et al. 2015, *MNRAS*, **452**, 1841
- Strauss, M. A., Weinberg, D. H., Lupton, R. H., et al. 2002, *ApJ*, **124**, 1810
- Surana, S., Wadadekar, Y., Bait, O., et al. 2020, *MNRAS*, **493**, 4808
- Sureshkumar, U., Durkalec, A., Pollo, A., et al. 2023, *A&A*, **669**, A27
- Takeuchi, T. T., Buat, V., Heinis, S., et al. 2010, *A&A*, **514**, A4
- Uhrig, R. E. 1995, in Proc. IECON 95—21st Annual Conf. on IEEE Industrial Electronics (Piscataway, NJ: IEEE), 33
- Viero, M. P., Asboth, V., Roseboom, I. G., et al. 2014, *ApJS*, **210**, 22
- Villar, V., Gallego, J., Pérez-González, P. G., et al. 2008, *ApJ*, **677**, 169
- Webb, S. A., & Goode, S. R. 2023, arXiv:2304.00512
- Wright, E. L., Eisenhardt, P. R. M., Mainzer, A. K., et al. 2010, *AJ*, **140**, 1868
- Wuyts, S., Förster Schreiber, N. M., Lutz, D., et al. 2011, *ApJ*, **738**, 106
- Yang, G., Boquien, M., Buat, V., et al. 2020, *MNRAS*, **491**, 740
- Yamamura, I., Makiuchi, S., Koga, T. & AKARI Team 2018, in The Cosmic Wheel and the Legacy of the AKARI Archive: From Galaxies and Stars to Planets and Life, ed. T. Ootsubo, 227
- Zeraatgari, F. Z., Hafezianzadeh, F., Zhang, Y., et al. 2024a, *MNRAS*, **527**, 4677
- Zeraatgari, F. Z., Hafezianzadeh, F., Zhang, Y.-X., et al. 2024b, *A&A*, **688**, A33